

# Nuclear temperature of spectator source extracted by neutron spectra in $^{124}\text{Sn}$ , $^{107}\text{Sn} + ^{120}\text{Sn}$ collisions at 600 MeV/nucleon

Huixiao Duan, Fan Zhang<sup>a</sup>, Kailei Wang

*Department of Physics,  
Changzhi University,  
Changzhi 046011, China*

(Dated: December 9, 2024)

## Abstract

The properties of neutrons from spectator sources produced in  $^{107,124}\text{Sn} + ^{120}\text{Sn}$  collisions at 600 MeV/nucleon are studied. The isospin-dependent quantum molecular dynamics (IQMD) model is used to describe the dynamical process of the fragmentation, and the statistical model GEMINI is applied to simulate the secondly decay of the pre-fragments. The differential cross section and multiplicity of the neutrons emitted from the spectator source are used to prove the feasibility of the model. The temperatures of the projectile-like source are extracted by fitting the transverse momentum distributions of the neutrons using the classical Maxwellian functions. The temperatures extracted from calculations are overall higher than the experimental data, but are consistent with those from the SMM model, and the isotopic temperature  $T_{\text{HeLi}}$ . Our work suggests the possible systematic errors in the experimental data of neutron spectra, which is of reference for the further development of neutron detector for heavy ion collisions at intermediate energies.

---

<sup>a</sup> zhangfan@mail.bnu.edu.cn

## I. INTRODUCTION

The study of nuclear properties under extreme conditions has long been a focal point of research [1]. These studies are crucial for understanding astrophysical and nuclear physics-related issues [2–4]. The heavy-ion collisions at intermediate energies are commonly used to study thermodynamic properties of the thermal nuclei at high temperature and density [5–7]. Thereinto, the hot nuclear system with excitation energy in the range of 3–8 MeV/A is applied to study the nuclear liquid-gas phase transition [8, 9]. Pochodzalla et al. used Au + Au peripheral collisions to analyze the caloric curve and discovered a plateau in the nuclear temperature in the excitation-energy-region of 3–8 MeV/A, a phenomenon similar to the liquid-gas phase transition of water at 373.15 K. This finding is considered significant evidence of the liquid-gas phase transition in nuclei [10].

Isospin effects play a critical role in nuclear fragmentation reactions [11–13]. Research on isospin effects provides a new way to extract information on symmetry energy [14, 15]. Since the application of the concept of the caloric curve to atomic nuclei, a significant isotopic dependence of the caloric curve or the nuclear temperatures is expected [16, 17]. Related experiments have been explored. An example is the comprehensive study of the isospin dependence of projectile fragmentation in  $^{107}\text{Sn}$ ,  $^{124}\text{Sn}$ ,  $^{124}\text{La} + \text{Sn}$  at 600 MeV/nucleon at the GSI Schwerionen-Synchrotron. In 2009, the A/Z dependence of projectile fragmentation at relativistic energies was studied with the ALADIN forward spectrometer at SIS [18]. It is found that the isotope temperatures for the neutron-rich projectiles are slightly larger than those for the neutron-poor projectiles. Global fragmentation observables were published, showing the weak dependence on the projectile N/Z [19]. Based on the Z distributions of the largest fragment in spectator fragmentation, the deduced pseudocritical points are found to be only weakly dependent on the ratio of the fragmenting spectator source [20]. Recently, the Large-Area-Neutron-Detector LAND is used to measure the neutron emission in projectile fragmentation and explore the N/Z dependence of the identified neutron source [21].

For the interpretation of the data, various models have been developed to study the mechanisms of the fragmentation reaction [22]. Statistical models are based on the assumption that fragments produced in a collision arise from a system in thermal equilibrium, and have been applied widely to study the fragmentation. In 1999, Borderie et al. [23] used a quan-

tum statistical model based on the thermodynamic equilibrium to describe the properties of fragment products from the projectile in an Ar+Ni reaction with an incident energy of 95 MeV/A. Similarly, Ogul et al. [19] applied the statistical multifragmentation model to study the spectator fragment products and found that the model could effectively describe the distribution of spectator fragmentation products. However, many studies suggest that thermal nuclei produced in peripheral collisions only partially achieve thermodynamic equilibrium. In 2003, Colin et al. [24] studied the fragmentation process of spectators in heavy-ion collisions in the Fermi energy region using systems of different masses. They found that most of the spectator fragments did not satisfy thermodynamic equilibrium conditions. Zbiri et al. [25] used Au + Au collisions in the intermediate-energy region and studied the fragmentation products from both participants and spectators, and showed that the spectator fragmentation products did not achieve equilibrium in the dynamical degrees of freedom. Furthermore, Russotto et al. [26, 27], using heavy-ion collisions in the Fermi energy region, studied the emission probabilities of intermediate-mass fragments and found that the emission of these fragments involved both dynamical and statistical mechanisms.

On the other hand, dynamical models, such as the Isospin-dependent Quantum Molecular Dynamics (IQMD) model, focus on the microscopic dynamics of the collision and fragmentation process, considering factors such as nucleon-nucleon interactions and the evolution of the system in time [28]. The combination of microscopic dynamics and the statistical model allows for a more comprehensive description of the fragmentation process, including the transition from a dynamical to a statistical regime as the system evolves. Recent progress has been made in combining these models to better predict and describe the complex fragmentation patterns observed in peripheral collisions. For instance, in the works by Su et al., the IQMD model is used to study the non-equilibrium thermalization and fragmentation. The statistical code GEMINI is applied to simulate the second decay of the pre-fragments. The data about the intermediate-mass fragments (IMFs) in  $^{107,124}\text{Sn}$  and  $^{124}\text{La}$  projectile fragmentation have been successfully reproduced by the combining model [29–31].

In this work, the IQMD+GEMINI model is applied to study the properties of neutrons emitted from the spectator source produced in  $^{124}\text{Sn}$ ,  $^{107}\text{Sn}$  +  $^{120}\text{Sn}$  collisions at 600 MeV/nucleon. The paper is organized as follows. In Sec. II, we briefly describe the method. In Sec. III, we present both the results and discussions. Finally, a summary is given in Sec. IV.

## II. THEORETICAL FRAMEWORK

### A. Isospin-dependent quantum molecular dynamics model

The wave function for each nucleon in the IQMD model is represented by a Gaussian wave packet

$$\phi_i(\mathbf{r}, t) = \frac{1}{(2\pi L)^{3/4}} e^{-\frac{[\mathbf{r}-\mathbf{r}_i(t)]^2}{4L}} e^{\frac{i\mathbf{r}\cdot\mathbf{p}_i(t)}{\hbar}}, \quad (1)$$

where  $\mathbf{r}_i$  and  $\mathbf{p}_i$  are the average values of the positions and momenta of the  $i$ th nucleon, and  $L$  is related to the extension of the wave packet. The phase-space density of the system is given by

$$f(\mathbf{r}, \mathbf{p}, t) = \sum_{i=1}^N \frac{1}{(\pi\hbar)^3} e^{-\frac{[\mathbf{r}-\mathbf{r}_i(t)]^2}{2L}} e^{-\frac{[\mathbf{p}-\mathbf{p}_i(t)]^2 \cdot 2L}{\hbar^2}}. \quad (2)$$

The time evolution of the nucleons in the system are governed by Hamiltonian equations of motion,

$$\begin{aligned} \dot{\mathbf{r}}_i &= \nabla_{\mathbf{p}_i} H, \\ \dot{\mathbf{p}}_i &= -\nabla_{\mathbf{r}_i} H. \end{aligned} \quad (3)$$

The Hamiltonian of baryons consists of the kinetic energy, the Coulomb interaction, and the nuclear interaction. The nuclear interaction includes the local two-body and three-body interactions, the symmetry potential. The nuclear potential density is expressed as

$$V(\rho, \delta) = \frac{\alpha \rho^2}{2 \rho_0} + \frac{\beta}{\gamma + 1} \frac{\rho^{\gamma+1}}{\rho_0^\gamma} + \frac{C_{sp}}{2} \left( \frac{\rho}{\rho_0} \right)^{\gamma_i} \rho \delta^2, \quad (4)$$

where  $\rho_0$  is the normal density. The parameters used in the following work are  $\alpha = -356.00$  MeV,  $\beta = 303.00$  MeV,  $\gamma = 7/6$ ,  $C_{sp} = 38.06$  MeV and  $\gamma_i = 0.75$ .

Binary NN collisions are included. The elastic proton-proton scatterings, elastic neutron-neutron scatterings, elastic neutron-proton scatterings, and inelastic NN collisions are included. The cross section in free space depends on the energy and isospin, and the in-medium factor is also energy dependent and isospin dependent. The method of the phase space density constraint (PSDC) is taken into account. The Pauli blocking method related to the PSDC is necessary after we use the PSDC method to compensate for the fermionic feature.

## B. GEMINI

The output of the IQMD code are the hot fragments. In order to obtain the cold fragments, emission of light particles ( $Z < 3$ ) from hot fragments is performed by the statistical code GEMINI [32]. A Monte Carlo technique is employed to follow the decay chains until the excitation energy of the product is zero. The partial decay widths are taken from the Hauser-Feshbach formalism,

$$\Gamma_{J_2}(Z_1, A_1, Z_2, A_2) = \frac{2J_1 + 1}{2\pi\rho_0} \sum_{l=|J_0-J_2|}^{J_0+J_2} \int_0^{E^*-B-E_{rot}} T_l(\varepsilon) \rho_2(E^* - B - E_{rot} - \varepsilon, J_2) d\varepsilon \quad (5)$$

where  $l$  and  $\varepsilon$  are the orbital angular momentum and kinetic energy of the emitted particle,  $E_{rot}$  is the rotation plus deformation energy of the residual system,  $\rho_0$  and  $\rho_2$  are the level densities of the initial and residual systems, respectively, and  $T_l$  is the transmission coefficient.

## III. RESULTS AND DISCUSSION

### A. Properties of projectile spectator

The  $^{107,124}\text{Sn} + ^{120}\text{Sn}$  collision at 600 MeV/nucleon is simulated by the IQMD+GEMINI model. The fragments with  $Z = 3$  and neutrons are applied to extract the fragmenting source. Figure 1 shows the two-dimensional distribution of transverse and longitudinal momentum for  $Z = 3$  fragments. Two distinct emission sources are apparent in the figure: a target-like source around  $p_z = 0$  and a projectile-like source near  $p_z = 1200$  MeV/c. The distribution's hot spot center lies at a transverse momentum of 50 MeV/c, corresponding to a transverse kinetic energy of 1.3 MeV. This recoil kinetic energy, influenced by both the emission source recoil and Coulomb repulsion of the fragments, is minor compared to the incident kinetic energy of 600 MeV/nucleon.

The blue line in the figure represents the emission angle of the fragments in the laboratory system. The acceptance range of the ALADIN spectrometer covers areas with horizontal angle less than  $10.2^\circ$  and vertical angle less than  $4.5^\circ$ . In the Ref. [21], the horizontal and vertical axes are designated as  $y$  and  $x$ , respectively, with the beam direction defined as  $z$ . In the experiment, it is not possible to explicitly identify the collision parameter direction.

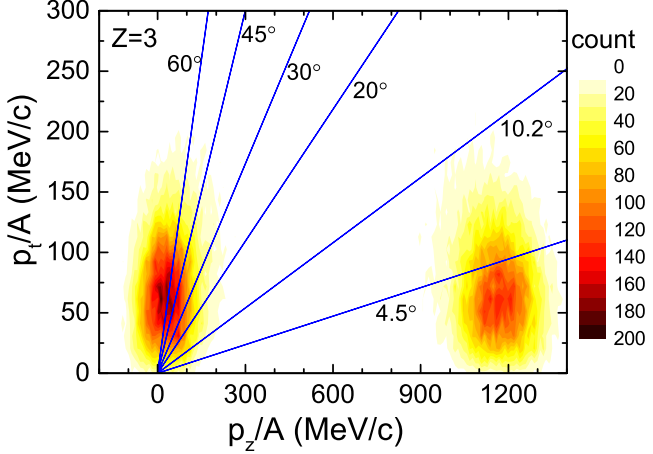


FIG. 1. Distribution of fragments with  $Z=3$  in the plane of transverse momentum  $p_t$  versus longitudinal momentum  $p_z$  for  $^{124}\text{Sn} + ^{120}\text{Sn}$  collision at 600 MeV/nucleon. The blue lines emitting angles in the laboratory frame. The values  $10.2^\circ$  and  $4.5^\circ$  are the maximum acceptance of the ALADIN forward spectrometer in the horizontal direction and in the vertical direction, respectively. The

Instead, the horizontal ( $y$ ) and vertical ( $x$ ) directions are defined by the detector orientation. This axis definition differs from theoretical studies, where the beam incidence direction is typically denoted as  $z'$ , the collision parameter direction as  $x'$ , and the perpendicular direction as  $y'$ . However, this discrepancy does not affect our analysis due to the relatively small recoil kinetic energy. Given the small recoil kinetic energy, the fragment emission shows axial symmetry along the  $z$ -axis. Thus variations in Cartesian coordinate definitions within the plane perpendicular to  $z$  do not impact the dynamic analysis.

The ALADIN spectrometer is designed to detect most of the fragments from projectile-like sources while excluding most of the those from the target-like emission sources. The horizontal acceptance angle of  $10.2^\circ$  is large enough to collect most fragments from the projectile-like sources, while the vertical acceptance angle of  $4.5^\circ$  is not enough. Some fragments with  $Z = 3$  have emission angles greater than  $4.5^\circ$  are not detected. This issue is more clearly illustrated by the angular distribution shown in Fig. 2. In the figure, the blue box represents the acceptance region of the ALADIN spectrometer, which extends  $\pm 10.2^\circ$  horizontally and  $\pm 4.5^\circ$  vertically.

In Ref. [19], it is reported that the ALADIN spectrometer captures 90% of  $Z = 3$  fragments. However, our calculations indicate a efficiency of only 74%. This discrepancy is

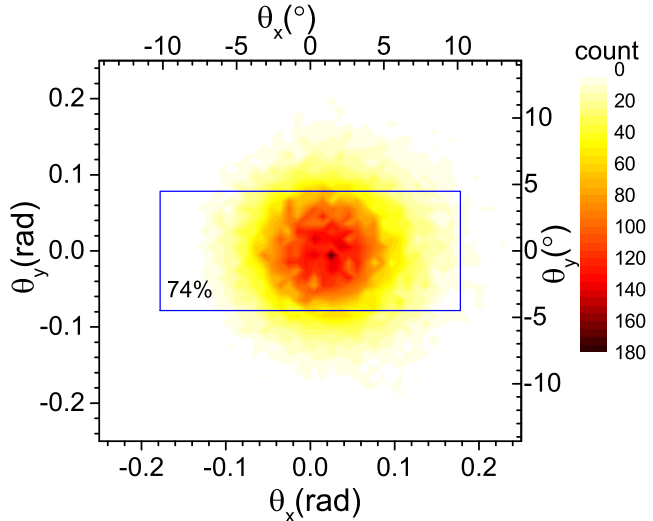


FIG. 2. Probability distribution with respect to the beam direction of the fragment with  $Z=3$  produced in  $^{124}\text{Sn} + ^{120}\text{Sn}$  collision at 600 MeV/nucleon. The blue square represents the acceptance-area of the ALADIN detector.

largely due to the recoil effect from the emission source, which impacts the vertical acceptance angle, though the horizontal acceptance angle is sufficiently large. Some fragments escape detection along the horizontal axis. The deviation between experimental and calculated reception efficiencies stems from an overestimation of the emitter temperature in the IQMD+GEMINI model used for simulations. It should be noted that the reception efficiency increases with the mass number of the emission source, eventually approaching 100% for heavier sources. Therefore, this deviation has a minimal effect on the subsequent discussion of the value of the bounding charge  $Z_{\text{bound}}$ .

Figure 3 shows distribution of neutrons in the plane of transverse momentum  $p_t$  versus longitudinal momentum  $p_z$ . Neutrons near  $p_z = 0$  originate from the target-like system, while those near  $p_z = 1200$  MeV/c come from the projectile-like system. A significant number of neutrons are also distributed over a broad range around  $p_z = 600$  MeV/c, which are emitted from the participants that acquire substantial transverse momentum due to the intense collision dynamics.

Neutrons can be emitted throughout the entire heavy-ion collision process, from the pre-equilibrium stage (characterized by violent two-body collisions), to the high-temperature stage of multiple fragmentation, and finally to the lower-temperature stage of secondary decay. In contrast, the  $Z = 3$  fragments (shown in Fig. 1) primarily originate from the

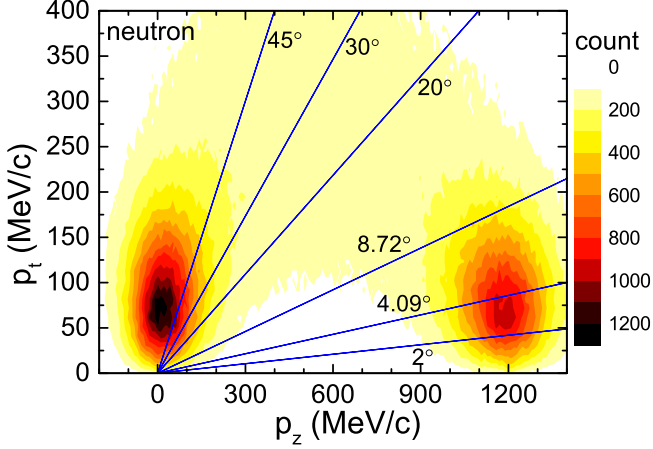


FIG. 3. Distribution of neutrons in the plane of transverse momentum  $p_t$  versus longitudinal momentum  $p_z$  for  $^{124}\text{Sn} + ^{120}\text{Sn}$  collision at 600 MeV/nucleon. The blue lines show emitting angles in the laboratory frame. The values  $8.72^\circ$  and  $4.09^\circ$  are the maximum acceptance of the LAND in the horizontal direction and in the vertical direction, respectively.

multiple fragmentation stage. This results in a wider kinetic energy distribution for the neutrons compared to the  $Z = 3$  fragments.

The blue line in the figure represents the neutron emission angle. It is shown in Ref. [21] that the maximum horizontal acceptance angle of the LAND is  $8.72^\circ$ , and the maximum vertical acceptance angle is  $4.09^\circ$ . It is clear that the LAND can effectively exclude most neutrons from both the target-like and participant systems.

Figure 4 shows the angular distribution of neutrons in the detector's receiving plane. The blue box represents the LAND's acceptance region. The center of the neutron distribution is at the origin, and the distribution is circular. The LAND covers the angular range  $0 < \theta_x < 8.72^\circ$  and  $-4.09^\circ < \theta_y < 4.09^\circ$ . The detector does not cover the region where  $\theta_x > 0^\circ$ . However, due to the symmetry of the system, this limitation does not adversely affect the results. In Ref. [21], a neutron emission source with a temperature of 4 MeV was studied, and it was found that LAND's acceptance for neutrons is 42.4%. However, the model calculations show that the LAND's acceptance is lower than this value for neutrons emitted by the bystander emission sources in the reaction.

The energy spectrum of neutrons with emission angles less than  $2^\circ$  has been measured in Ref. [21]. The calculated energy spectrum by the IQMD+GEMINI model is compared with the experimental data in Figure 5. The dashed line in the figure represents an incident

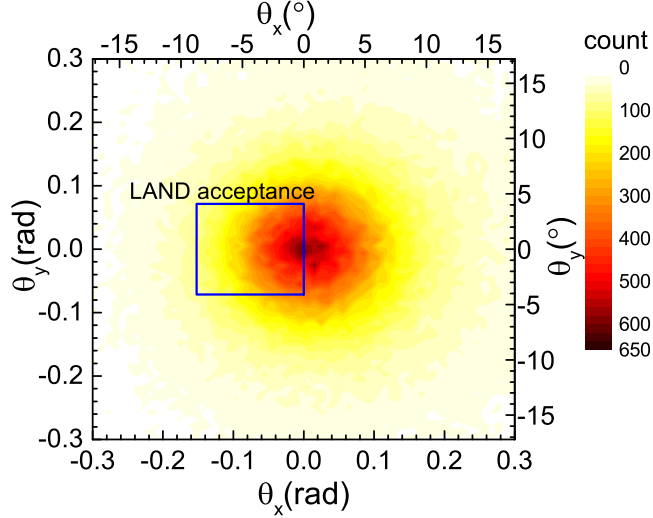


FIG. 4. Probability distribution with respect to the beam direction of neutron produced in  $^{124}\text{Sn} + ^{120}\text{Sn}$  collision at 600 MeV/nucleon. The blue square represents the acceptance-area of the LAND.

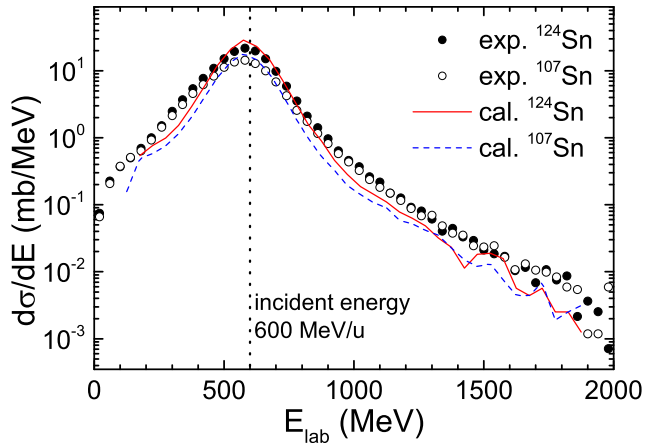


FIG. 5. Inclusive differential cross section of neutrons in the laboratory detected within the solid angle  $\theta_{\text{lab}} < 2^\circ$  for the  $^{107,124}\text{Sn} + ^{120}\text{Sn}$  collisions at 600 MeV/nucleon. The experimental data are taken from Ref. [21].

energy of 600 MeV/u. Both the experimental and calculated spectra show a peak of the differential cross section at 600 MeV/u, indicating that neutrons emitted at angles less than  $2^\circ$  primarily originate from projectile-like emission sources, with a minimal recoil effect.

The experimental energy spectra for the  $^{124}\text{Sn}$  and  $^{107}\text{Sn}$  systems have similar shapes, but the cross section for the  $^{124}\text{Sn}$  system is slightly larger than that for  $^{107}\text{Sn}$ . For the  $^{124}\text{Sn}$  system, the peak value is 21.7 mb/MeV, while for the  $^{107}\text{Sn}$  system, the peak value

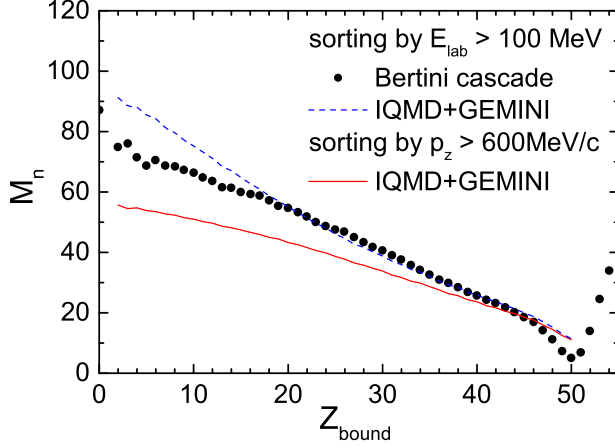


FIG. 6. Neutron multiplicity as a function of  $Z_{\text{bound}}$  for  $^{124}\text{Sn} + ^{120}\text{Sn}$  collision at 600 MeV/nucleon. The circles are the calculations by the Bertini cascade implemented in GEANT4 taken from Ref. [21].

is 4.3 mb/MeV. The calculations capture the overall shape and system dependence of the experimental energy spectrum: the peak occurs at 600 MeV, and the peak for the  $^{124}\text{Sn}$  system is larger than for the  $^{107}\text{Sn}$  system. However, the energy spectrum predicted by the model is somewhat narrower than the experimental spectrum.

The GEANT4 toolkit was used in Ref. [21] to simulate a  $^{124}\text{Sn}$  beam at 600 MeV/u incident on a 0.5 mm thick Sn target, calculating neutron multiplicity as a function of  $Z_{\text{bound}}$ , as shown by the dots in Fig. 6. The GEANT4 simulations employ the Bertini cascade model. In the calculations, neutrons emitted from secondary de-excitations of target fragments were excluded by applying the condition  $E_{\text{lab}} > 100$  MeV. Following this criterion, we obtained the neutron multiplicity as a function of  $Z_{\text{bound}}$  from the IQMD+GEMINI model, represented by the blue curve in Fig. 6.

In the range  $20 < Z_{\text{bound}} < 45$ , the IQMD+GEMINI model and the Bertini cascade model yield closely matching results. Differences appear, however, in peripheral and central collision regions. For peripheral collisions, the neutron multiplicity predicted by the Bertini cascade model is lower than that predicted by the IQMD+GEMINI model. At  $Z_{\text{bound}} = 50$ , the cascade model gives a neutron multiplicity of 4, while the IQMD+GEMINI model predicts 11. This discrepancy reflects differences in the predicted isotopic distribution of Sn fragments: the IQMD+GEMINI model suggests more neutron-deficient isotopes. If only quasi-projectile fragments are considered, the maximum  $Z_{\text{bound}}$  should be 50. However,

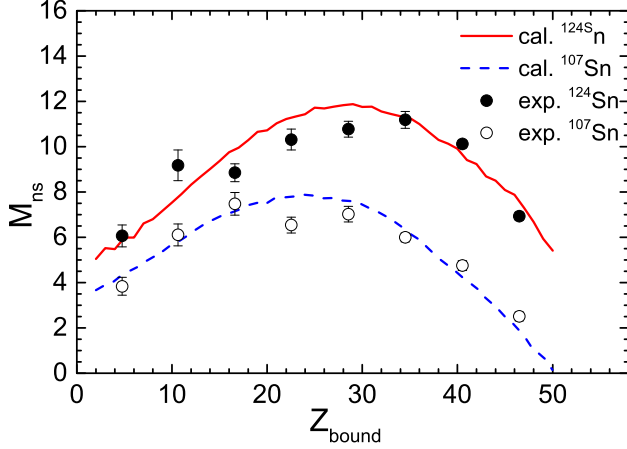


FIG. 7. Neutron multiplicity of the projectile source as a function of  $Z_{\text{bound}}$  for  $^{107,124}\text{Sn} + ^{120}\text{Sn}$  collision at 600 MeV/nucleon. The neutrons from the projectile source are sorted by  $1000 \text{ MeV}/c < p_z < 1500 \text{ MeV}/c$ . The experimental data are taken from Ref. [21].

the cascade model shows calculation even for  $Z_{\text{bound}} > 50$ , possibly due to the method for selecting quasi-projectile fragments.

In central collisions, neutron multiplicity steadily increases as  $Z_{\text{bound}}$  decreases. For instance, at  $Z_{\text{bound}} = 2$ , the cascade model predicts a neutron multiplicity near 80, while the IQMD+GEMINI model suggests a higher count, reaching 91 free neutrons. Notably, using  $E_{\text{lab}} > 100 \text{ MeV}$  to filter for neutrons from projectile fragmentation is not the optimal method. As shown in Fig. 3, the single-nucleon momentum of the projectile is approximately 1200 MeV/c in the experimental frame. Applying a transverse momentum filter of  $p_z > 600 \text{ MeV}/c$  more effectively selects neutrons originating from projectile fragmentation.

The neutron multiplicity filtered by  $p_z > 600 \text{ MeV}/c$  is depicted by the red curve in Fig. 6. This criterion selects fewer neutrons than the  $E_{\text{lab}} > 100 \text{ MeV}$  threshold. At  $Z_{\text{bound}} = 2$ , neutron multiplicity reaches 59, indicating that for central collisions, 59 of the 70 neutrons in the  $^{124}\text{Sn}$  projectile are released as free neutrons, while the remaining 11 are emitted as deuterons or tritons.

In fact, the neutrons selected using the condition  $p_z > 600 \text{ MeV}/c$  do not originate from a single equilibrated thermal source. During the early stages of projectile-target collisions, neutrons are emitted from one side of the projectile due to intense collisions. These neutrons are associated with the participant zone and exhibit a higher temperature. After the violent collision process ends, part of the projectile is sheared off, leaving an excited remnant (i.e.,

the spectator source), which de-excites through nucleon emission and multi-fragmentation. By isolating this subset of neutrons, the momentum distribution of the neutrons can provide insights into the spectator source characteristics. In Ref. [21], the condition  $1000 \text{ MeV}/c < p_z < 1500 \text{ MeV}/c$  is used to select neutrons originating from the spectator source. We used the same method to extract neutrons originating from the spectator source. Figure 7 shows the experimental and theoretical neutron multiplicity as a function of  $Z_{\text{bound}}$ . Experimental data indicate that as  $Z_{\text{bound}}$  increases, the neutron multiplicity first rises and then falls. This trend is similar to the variation in intermediate-mass fragment (IMF) multiplicity with  $Z_{\text{bound}}$ . For events around  $Z_{\text{bound}} \approx 30$ , the spectator source primarily undergoes multifragmentation during de-excitation, leading to the emission of a larger number of neutrons. In contrast, for events with smaller or larger  $Z_{\text{bound}}$ , the spectator source is either smaller or has lower excitation energy, resulting in fewer emitted neutrons.

Comparing the results for the  $^{124}\text{Sn}$  and  $^{107}\text{Sn}$  projectiles reveals that  $^{124}\text{Sn}$  leads to a neutron-rich spectator, producing higher neutron multiplicity. Conversely,  $^{107}\text{Sn}$  results in a neutron-deficient spectator, yielding lower neutron multiplicity. However, the difference in neutron multiplicity between the two systems is approximately 4, which is smaller than the neutron number difference of 17 between  $^{124}\text{Sn}$  and  $^{107}\text{Sn}$ . This suggests that during the violent collision stage, before the formation of the equilibrated spectator source, the excess neutrons in  $^{124}\text{Sn}$  are largely emitted, causing the neutron multiplicities of the spectator sources in both systems to converge.

Comparing the IQMD+GEMINI model calculations with experimental data shows a high degree of consistency. Combined with the multiplicity observables reported in the literature, we can conclude that the IQMD+GEMINI model accurately captures the primary features of the collision dynamics in  $^{124}\text{Sn} + ^{120}\text{Sn}$  reactions. This provides a reliable foundation for the subsequent analysis of the spectator source temperature.

We adopted the same method and calculated the transverse momentum distribution of these neutrons, as shown in Fig. 8. The full circles is the experimental data. The (blue) open circles and (red) open square are the calculated distributions of  $p_y$  and  $p_x$ , respectively. The neutron density distribution in the  $p_y$  vs  $p_x$  plane is assumed to be classical Maxwellian function added to a constant background pedestal.

$$\frac{\partial^2 N}{\partial p_x \partial p_y} = C_1 \exp\left(-\frac{p_x^2}{2mT_x^2}\right) \exp\left(-\frac{p_y^2}{2mT_y^2}\right) + C_2. \quad (6)$$

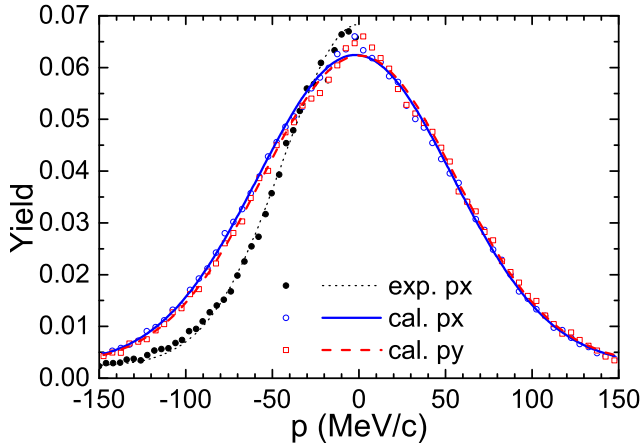


FIG. 8. Distribution of transverse momentum for neutrons from the fragmentation of  $^{124}\text{Sn}$  projectiles, selected with the condition  $Z_{\text{bound}} \leq 45$ . The full circles and the dotted curve are the experimental data and corresponding fit. The (blue) open circles and (red) open square are the calculated distributions of  $p_x$  and  $p_y$ , respectively. The corresponding fits are shown as (blue) curve and (red) dash. The data are taken from Ref. [21].

where  $m$  is the neutron mass,  $C_1$  and  $C_2$  are the fitting parameters,  $T_x$  and  $T_y$  are the temperature parameters. To find the temperature parameter, the distribution of  $p_x$  (or  $p_y$ ) is fitted. The fit of experimental data with a Gaussian distribution corresponding to  $T_x = 2.04$  MeV superimposed on a constant background is represented by the dotted line. The cases for the calculated  $p_x$  and  $p_y$  distributions are shown as (blue) curve and (red) dash. The corresponding temperature parameters are  $T_x = 3.37$  MeV and  $T_y = 3.31$  MeV, which are significantly higher than the experimental value.

The variation of temperature with  $Z_{\text{bound}}$ , extracted from momentum distributions, is shown in Fig. 9. The experimental data are represented by open circles and open triangles, while the IQMD+GEMINI model calculations are shown as curves and short dashed lines. The temperature display a weak isospin effect, where the temperature of the  $^{124}\text{Sn}$  system is slightly higher than that of the  $^{107}\text{Sn}$  system. This result is consistent with findings in Ref. [18], and the specific reasons will not be elaborated here.

A key issue in the figure is why the temperatures extracted from neutron momentum distributions calculated by the IQMD+GEMINI model are overall higher than the experimental data. The figure shows that as  $Z_{\text{bound}}$  increases from 5 to 45, the temperature extracted from experimental data decreases from 5 MeV to 3 MeV, while the temperature calculated

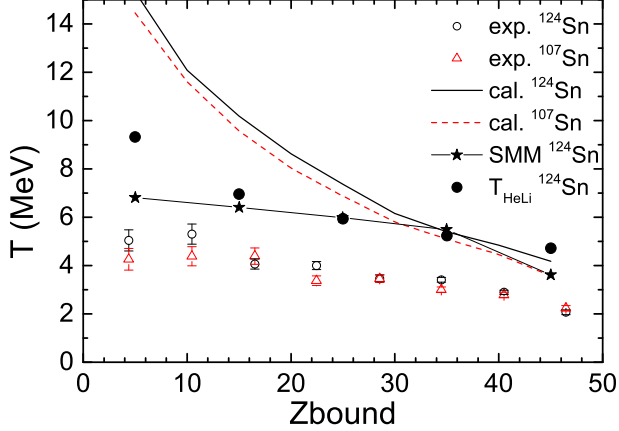


FIG. 9. Temperature of the projectile source as a function of  $Z_{\text{bound}}$  for  $^{107,124}\text{Sn} + ^{120}\text{Sn}$  collision at 600 MeV/nucleon. The isotopic temperatures  $T_{\text{HeLi}}$  extracted from experimental data in Ref. [18] is also included. The temperatures extracted from the experimental neutron spectra and the calculations by the SMM model are taken from Ref. [21].

by the IQMD+GEMINI model decreases from 15 MeV to 4 MeV.

First, for the  $^{124}\text{Sn} + ^{120}\text{Sn}$  system at 600 MeV/u, the IQMD+GEMINI model has relatively low systematic uncertainty. In Ref. [29] the IQMD+GEMINI model is applied to study the dynamical features of this reaction and successfully reproduces observables such as intermediate-mass fragment multiplicity. In Ref. [31] it is applied to explores the fluctuation characteristics in this reaction.

Second, in the region  $Z_{\text{bound}} > 25$ , the IQMD+GEMINI model results are consistent with those from the SMM model (shown as stars). Ref. [21] demonstrates that the SMM model cannot fully reproduce the experimentally measured neutron multiplicity. In the  $Z_{\text{bound}} < 25$  region, the SMM model underestimates neutron multiplicity.

Finally, compared to  $T_{\text{HeLi}}$  (shown as full circles), the temperature parameter extracted from product momentum distributions should be higher. Based on the above analysis, we speculate that the emission source temperature measured in Ref. [21], based on neutron momentum distributions, may have systematic errors that require further investigation.

#### IV. CONCLUSION

In summary, the  $^{107,124}\text{Sn} + ^{120}\text{Sn}$  collisions at 600 MeV/nucleon are studied by the IQMD+GEMINI model. The two-dimensional distribution of transverse and longitudinal momentum for fragments with  $Z = 3$  and neutrons are applied to show the emission sources. It is shown that only target-like and projectile-like emission sources are apparent for the  $Z = 3$  fragments, but the contribution of the participant source is considerable for neutrons. The recoil kinetic energy of the projectile-like source is minor compared to its kinetic energy near 600 MeV/nucleon.

The calculations of the differential cross section, multiplicity, transverse momentum distribution of neutrons from the projectile-like source are compared with the data taken from Ref. [21]. It is found that the calculations shows a high degree of consistency with the data of differential cross section and multiplicity as a function of the bounding charge. For the transverse momentum distribution, the calculations capture the Gaussian shape, but the calculated distribution width is larger than the experimental case.

The temperatures of the projectile-like source are extracted by fitting the transverse momentum distributions using the classical Maxwellian functions. The temperature display a weak isospin effect, where the temperature of the  $^{124}\text{Sn}$  system is slightly higher than that of the  $^{107}\text{Sn}$  system. This result is consistent with findings in Ref. [18]. The temperatures extracted from calculations are overall higher than the experimental data, but are consistent with those from the SMM model taken from Ref. [21], and the isotopic temperature  $T_{\text{HeLi}}$  taken from Ref. [18]. It is speculated that the emission source temperature extracted based on neutron momentum distributions may have systematic errors that require further investigation.

#### ACKNOWLEDGMENTS

This work was supported by the National Natural Science Foundation of China under Grants No. 12205026 and Applied Basic Research Program of Shanxi Province, China under

Grant Nos. 202103021223376 and 202203021212171.

---

- [1] P. Braun-Munzinger, V. Koch, T. Schäfer, and J. Stachel, Physics Reports **621**, 76 (2016).
- [2] X.-B. Wei, H.-L. Wei, Y.-T. Wang, J. Pu, K.-X. Cheng, Y.-F. Guo, and C.-W. Ma, Nuclear Science and Techniques **33**, 155 (2022).
- [3] J.-F. Xu, C.-J. Xia, Z.-Y. Lu, G.-X. Peng, and Y.-P. Zhao, Nuclear Science and Techniques **33**, 143 (2022).
- [4] W.-J. Xie, Z.-W. Ma, and J.-H. Guo, Nuclear Science and Techniques **34**, 91 (2023).
- [5] C. Liu, X.-G. Deng, and Y.-G. Ma, Nuclear Science and Techniques **33**, 52 (2022).
- [6] K. Xiao, P.-C. Li, Y.-J. Wang, F.-H. Liu, and Q.-F. Li, Nuclear Science and Techniques **34**, 62 (2023).
- [7] G.-Y. Cheng, Q.-M. Su, X.-G. Cao, and G.-Q. Zhang, Nuclear Science and Techniques **35**, 33 (2024).
- [8] J. Zhang, H.-M. Liu, Z.-H. Li, G. Burgio, and H.-J. Schulze, Chinese Physics C **46**, 114105 (2022).
- [9] E. Xiao, X. Lei, Y. Huang, Y. Feng, L. Zhu, and J. Su, Chinese Physics C **48**, 014104 (2024).
- [10] J. Pochodzalla, T. Möhlenkamp, T. Rubehn, A. Schüttauf, A. Wörner, E. Zude, M. Begemann-Blaich, T. Blaich, H. Emling, A. Ferrero, *et al.*, Physical review letters **75**, 1040 (1995).
- [11] D. Peng, C.-W. Ma, C.-Y. Qiao, X.-Q. Liu, and H.-L. Wei, Chinese Physics C **48**, 064103 (2024).
- [12] X.-D. Xu, Y.-Z. Sun, S.-T. Wang, B. Mei, S.-Y. Jin, X.-H. Zhang, Z.-Y. Sun, Y.-X. Zhao, S.-W. Tang, Y.-H. Yu, *et al.*, Chinese Physics C **46**, 111001 (2022).
- [13] S.-Y. Jin, Y.-Z. Sun, S.-T. Wang, Z.-Y. Sun, X.-H. Zhang, Z.-Q. Chen, B. Mei, Y.-X. Zhao, S.-W. Tang, Y.-H. Yu, *et al.*, Chinese Physics C **46**, 014003 (2022).
- [14] L. Li, F.-Y. Wang, and Y.-X. Zhang, Nuclear Science and Techniques **33**, 58 (2022).
- [15] F.-Y. Wang, J.-P. Yang, X. Chen, Y. Cui, Y.-J. Wang, Z.-G. Xiao, Z.-X. Li, and Y.-X. Zhang, Nuclear Science and Techniques **34**, 94 (2023).
- [16] A. Kelić, J. B. Natowitz, and K. H. Schmidt, in *Dynamics and Thermodynamics with Nuclear Degrees of Freedom* (Springer, 2006) pp. 203–213.

[17] A. . COLLABORATION, W. TRAUTMANN, P. ADRICH, T. AUMANN, C. BACRI, T. BARCZYK, R. BASSINI, S. BIANCHIN, C. BOIANO, A. BOTVINA, *et al.*, International Journal of Modern Physics E **17**, 1838 (2008).

[18] C. Sfienti, P. Adrich, T. Aumann, C. Bacri, T. Barczyk, R. Bassini, S. Bianchin, C. Boiano, A. Botvina, A. Boudard, *et al.*, Physical Review Letters **102**, 152701 (2009).

[19] R. Ogul, A. Botvina, U. Atav, N. Buyukcizmeci, I. Mishustin, P. Adrich, T. Aumann, C. Bacri, T. Barczyk, R. Bassini, *et al.*, Physical Review CNuclear Physics **83**, 024608 (2011).

[20] T. Pietrzak, A. Botvina, J. Brzychczyk, N. Buyukcizmeci, A. Le Fèvre, J. Lukasik, P. Pawłowski, C. Sfienti, W. Trautmann, and A. Wieloch, Physics letters B **809**, 135763 (2020).

[21] P. Pawłowski, J. Brzychczyk, N. Buyukcizmeci, H. Johansson, W. Trautmann, A. Wieloch, P. Adrich, T. Aumann, T. Barczyk, S. Bianchin, *et al.*, Physical Review C **108**, 044610 (2023).

[22] J. Richert and P. Wagner, Physics Reports **350**, 1 (2001).

[23] I. Collaboration, B. Borderie, F. Gulminelli, M. Rivet, L. Tassan-Got, M. Assenard, G. Auger, F. Bocage, R. Bougault, R. Brou, *et al.*, The European Physical Journal A-Hadrons and Nuclei **6**, 197 (1999).

[24] J. Colin, D. Cussol, J. Normand, N. Bellaize, R. Bougault, A. Buta, D. Durand, O. Lopez, L. Manduci, J. Marie, *et al.*, Physical Review C **67**, 064603 (2003).

[25] K. Zbiri, A. L. Fèvre, J. Aichelin, J. Łukasik, W. Reisdorf, F. Gulminelli, U. Lynen, W. Müller, H. Orth, C. Schwarz, *et al.*, Physical Review CNuclear Physics **75**, 034612 (2007).

[26] P. Russotto, E. De Filippo, A. Pagano, L. Acosta, L. Auditore, V. Baran, I. Berceanu, B. Borderie, R. Bougault, M. Bruno, *et al.*, Physical Review C **91**, 014610 (2015).

[27] P. Russotto, E. De Filippo, E. Pagano, L. Acosta, L. Auditore, T. Cap, G. Cardella, S. De Luca, E. Geraci, B. Gnoffo, *et al.*, The European Physical Journal A **56**, 12 (2020).

[28] C. Hartnack, R. K. Puri, J. Aichelin, J. Konopka, S. Bass, H. Stoecker, and W. Greiner, The European Physical Journal A-Hadrons and Nuclei **1**, 151 (1998).

[29] J. Su, W. Trautmann, L. Zhu, W.-J. Xie, and F.-S. Zhang, Physical Review C **98**, 014610 (2018).

[30] J. Su, L. Zhu, C. Guo, and Z. Zhang, Physical Review C **100**, 014602 (2019).

[31] E. Xiao, Y. Feng, X. Lei, L. Zhu, and J. Su, Journal of Physics G: Nuclear and Particle Physics **49**, 065102 (2022).

[32] R. Charity, M. McMahan, G. Wozniak, R. McDonald, L. Moretto, D. Sarantites, L. Sobotka, G. Guarino, A. Pantaleo, L. Fiore, *et al.*, Nuclear Physics A **483**, 371 (1988).